

High-efficiency degenerate four wave-mixing in triply resonant nanobeam cavities

Zin Lin^{1,*}, Thomas Alcorn², Marko Loncar¹, Steven G. Johnson², and Alejandro W. Rodriguez³

¹*School of Engineering and Applied Sciences, Harvard University, Cambridge, MA 02138*

²*Department of Mathematics, Massachusetts Institute of Technology, Cambridge, MA 02139 and*

³*Department of Electrical Engineering, Princeton University, Princeton, NJ, 08544*

(Dated: July 25, 2018)

We demonstrate high-efficiency, degenerate four-wave mixing in triply resonant Kerr ($\chi^{(3)}$) photonic crystal (PhC) nanobeam cavities. Using a combination of temporal coupled mode theory and nonlinear finite-difference time-domain (FDTD) simulations, we study the nonlinear dynamics of resonant four-wave mixing processes and demonstrate the possibility of observing high-efficiency limit cycles and steady-state conversion corresponding to $\approx 100\%$ depletion of the pump light at low powers, even including effects due to losses, self- and cross-phase modulation, and imperfect frequency matching. Assuming operation in the telecom range, we predict close to perfect quantum efficiencies at reasonably low $\sim 50\text{mW}$ input powers in silicon micrometer-scale cavities.

PACS numbers: Valid PACS appear here

I. INTRODUCTION

Optical nonlinearities play an important role in numerous photonic applications, including frequency conversion and modulation [1–7], light amplification and lasing [1, 8–10], beam focusing [1, 11], phase conjugation [1, 12], signal processing [13, 14], and optical isolation [15, 16]. Recent developments in nanofabrication are enabling fabrication of nanophotonic structures, e.g. waveguides and cavities, that confine light over long times and small volumes [17–21], minimizing the power requirements of nonlinear devices [22, 23] and paving the way for novel on-chip applications based on all-optical nonlinear effects [18, 24–33]. In addition to greatly enhancing light–matter interactions, the use of cavities can also lead to qualitatively rich dynamical phenomena, including multistability and limit cycles [34–40]. In this paper, we explore realistic microcavity designs that enable highly efficient degenerate four-wave mixing (DFWM) beyond the undepleted pump regime. In particular, we extend the results of our previous work [41], which focused on the theoretical description of DFWM in triply resonant systems via the temporal coupled-mode theory (TCMT) framework, to account for various realistic and important effects, including linear losses, self- and cross-phase modulation, and frequency mismatch. Specifically, we consider the nonlinear process depicted in Fig. 1, in which incident light at two nearby frequencies, a pump ω_0 and signal $\omega_m = \omega_0 - \Delta\omega$ photon, is up-converted into output light at another nearby frequency, an idler $\omega_p = \omega_0 + \Delta\omega$ photon, inside a triply resonant photonic crystal nanobeam cavity (depicted schematically in Fig. 8). We demonstrate that 100% conversion efficiency (complete depletion of the pump power) can be achieved at a critical power and that detrimental effects associated with self- and cross-phase modulation can be overcome by appropriate tuning of the cavity resonances. Surprisingly, we find that critical solutions associated with maximal frequency conversion are ultra-sensitive to frequency mismatch (deviations from per-

fect frequency matching resulting from fabrication imperfections), but that there exist other robust, dynamical states (e.g. “depleted” states and limit cycles) that, when properly excited, can result in high conversion efficiencies at reasonable pump powers. We demonstrate realistic designs based on PhC nanobeam cavities that yield 100% conversion efficiencies at $\sim 50\text{mW}$ pump powers and over broad bandwidths (modal lifetimes $Q \sim 1000\text{s}$). Although our cavity designs and power requirements are obtained using the TCMT framework, we validate these predictions by checking them against rigorous, nonlinear FDTD simulations.

Although chip-scale nonlinear frequency conversion has been a topic of interest for decades [33], most theoretical and experimental works have been primarily focused on large-etalon and singly resonant systems exhibiting either large footprints and small bandwidths [25, 26, 42, 43], or low conversion efficiencies (the undepleted pump regime) [22, 44–46]. These include studies of $\chi^{(2)}$ processes such as second harmonic generation [26, 47–49], sum and difference frequency generation [50], and optical parametric amplification [27, 28, 51], as well as $\chi^{(3)}$ processes such as third harmonic generation [47, 52], four-wave mixing [53–55] and optical parametric oscillators [22, 56–58]. Studies that go beyond the undepleted regime and/or employ resonant cavities reveal complex nonlinear dynamics in addition to high efficiency conversion [23, 37–39, 41, 59, 60], but have primarily focused on ring resonator geometries due to their simplicity and high degree of tunability [60]. Significant efforts are underway to explore similar functionality in wavelength-scale photonic components (e.g. photonic crystal cavities) [49, 50], although high-efficiency conversion has yet to be experimentally demonstrated. Photonic crystal nanobeam cavities not only offer a high degree of tunability, but also mitigates the well-known volume and bandwidth tradeoffs associated with ring resonators [61], yielding minimal device footprint and on-chip integrability [62, 63], in addition to high quality factors [21, 64–67].

In what follows, we investigate the conditions and design criteria needed to achieve high efficiency DFWM in realistic nanobeam cavities. Our paper is divided into two primary sections. In Sec. II, we revisit the TCMT framework

*Electronic address: zlin@seas.harvard.edu

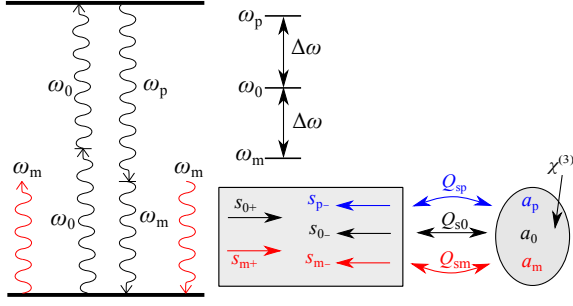


FIG. 1: Schematic diagram of a degenerate four-wave mixing process in which a pump photon at frequency ω_0 and a signal photon at frequency $\omega_m = \omega_0 - \Delta\omega$ are converted into an idler photon at $\omega_p = \omega_0 + \Delta\omega$ and an additional signal photon at ω_m , inside of a triply resonant $\chi^{(3)}$ nonlinear cavity. The cavity supports three resonant modes with frequencies ω_{ck} , lifetimes Q_k , and modal amplitudes a_k , which are coupled to a waveguide supporting propagating modes at the incident/output frequencies ω_k , with coupling lifetimes Q_{sk} . The incident and output powers associated with the k th mode are given by $|s_{k+}|^2$ and $|s_{k-}|^2$.

introduced in Ref. 41, and extend it to include new effects arising from cavity losses (Sec. II A), self- and cross-phase modulation (Sec. II B), and frequency mismatch (Sec. II C). In Sec. III, we consider specific designs, starting with a simple 2d design (Sec. III B) and concluding with a more realistic 3d design suitable for experimental realization (Sec. III C). The predictions of our TCMT are checked and validated in the 2d case against exact nonlinear FDTD simulations.

II. TEMPORAL COUPLED-MODE THEORY

In order to obtain accurate predictions for realistic designs, we extend the TCMT predictions of [41] to include important effects associated with the presence of losses, self- and cross-phase modulation, and imperfect frequency-matching. We consider the DFM process depicted in Fig. 1, in which incident light from some input/output channel (e.g. a waveguide) at frequencies ω_0 and ω_m is converted to output light at a different frequency $\omega_p = 2\omega_0 - \omega_m$ inside a triply-resonant $\chi^{(3)}$ cavity. The fundamental assumption of TCMT (accurate for weak nonlinearities) is that any such system, regardless of geometry, can be accurately described by a few set of geometry-specific parameters [41]. These include, the frequencies ω_{ck} and corresponding lifetimes τ_k (or quality factors $Q_k = \omega_{ck}\tau_k/2$) of the cavity modes, as well as nonlinear coupling coefficients, $\alpha_{kk'}$ and β_k , determined by overlap integrals between the cavity modes (and often derived from perturbation theory [23]). Note that in general, the total decay rate ($1/\tau_k$) of the modes consist of decay into the input/output channel ($1/\tau_{sk}$), as well as external (e.g. absorption or radiation) losses with decay rate $1/\tau_{ek}$, so that $1/\tau_k = 1/\tau_{sk} + 1/\tau_{ek}$. Letting a_k denote the time-dependent complex amplitude of the k th cavity mode (normalized so that $|a_k|^2$ is the electromagnetic energy stored in this mode), and letting $s_{k\pm}$ denote the time-dependent amplitude of the inci-

dent (+) and outgoing (−) light (normalized so that $|s_{k\pm}|^2$ is the power at the incident/output frequency ω_k), it follows that the field amplitudes are determined by the following set of coupled ordinary differential equations [23]:

$$\frac{da_0}{dt} = i\omega_{c0} (1 - \alpha_{00}|a_0|^2 - \alpha_{0m}|a_m|^2 - \alpha_{0p}|a_p|^2) a_0 - \frac{a_0}{\tau_0} - i\omega_{c0}\beta_0 a_0^* a_m a_p + \sqrt{\frac{2}{\tau_{s0}}} s_{0+}, \quad (1)$$

$$\frac{da_m}{dt} = i\omega_{cm} (1 - \alpha_{m0}|a_0|^2 - \alpha_{mm}|a_m|^2 - \alpha_{mp}|a_p|^2) a_m - \frac{a_m}{\tau_m} - i\omega_{cm}\beta_m a_0^2 a_p^* + \sqrt{\frac{2}{\tau_{sm}}} s_{m+}, \quad (2)$$

$$\frac{da_p}{dt} = i\omega_{cp} (1 - \alpha_{p0}|a_0|^2 - \alpha_{pm}|a_m|^2 - \alpha_{pp}|a_p|^2) a_p - \frac{a_p}{\tau_p} - i\omega_{cp}\beta_p a_0^2 a_m^*, \quad (3)$$

$$s_{0-} = \sqrt{\frac{2}{\tau_{s0}}} a_0 - s_{0+}, \quad s_{m-} = \sqrt{\frac{2}{\tau_{sm}}} a_m - s_{m+},$$

$$s_{p-} = \sqrt{\frac{2}{\tau_{sp}}} a_p, \quad (4)$$

where the nonlinear coupling coefficients [41],

$$\alpha_{kkk} = \frac{1}{8} \frac{\int d^3\mathbf{x} \epsilon_0 \chi^{(3)} [2|\mathbf{E}_k \cdot \mathbf{E}_k^*|^2 + |\mathbf{E}_k \cdot \mathbf{E}_k|^2]}{(\int d^3\mathbf{x} \epsilon |\mathbf{E}_k|^2)^2} \quad (5)$$

$$\alpha_{kkk'} = \frac{1}{4} \frac{\int d^3\mathbf{x} \epsilon_0 \chi^{(3)} [|\mathbf{E}_k \cdot \mathbf{E}_{k'}^*|^2 + |\mathbf{E}_k \cdot \mathbf{E}_{k'}|^2 + |\mathbf{E}_k|^2 |\mathbf{E}_{k'}|^2]}{(\int d^3\mathbf{x} \epsilon |\mathbf{E}_k|^2) (\int d^3\mathbf{x} \epsilon |\mathbf{E}_{k'}|^2)} \quad (6)$$

$$\alpha_{kkk'} = \alpha_{k'kk} \quad (7)$$

$$\beta_0 = \frac{1}{4} \frac{\int d^3\mathbf{x} \epsilon_0 \chi^{(3)} [(\mathbf{E}_0^* \cdot \mathbf{E}_0^*)(\mathbf{E}_m \cdot \mathbf{E}_p) + 2(\mathbf{E}_0^* \cdot \mathbf{E}_m)(\mathbf{E}_0^* \cdot \mathbf{E}_p)]}{(\int d^3\mathbf{x} \epsilon |\mathbf{E}_0|^2) (\int d^3\mathbf{x} \epsilon |\mathbf{E}_m|^2)^{1/2} (\int d^3\mathbf{x} \epsilon |\mathbf{E}_p|^2)^{1/2}} \quad (8)$$

$$\beta_m = \beta_p = \beta_0^*/2 \quad (9)$$

express the strength of the nonlinearity for a given mode, with the α terms describing SPM and XPM effects and the β terms characterizing energy transfer between the modes. (Technically speaking, this qualitative distinction between α and β is only true in the limit of small losses [23]).

A. Losses

Eqs. 1–4 can be solved to study the steady-state conversion efficiency of the system [$\eta = |s_{p-}|^2 / (|s_{0+}|^2 + |s_{m+}|^2)$] in response to incident light at the resonant cavity frequencies ($\omega_k = \omega_{ck}$), as was done in Ref. 41 in the ideal case of perfect frequency-matching ($\omega_{cp} = 2\omega_{c0} - \omega_{cm}$), no losses ($\tau_k \neq \tau_{sk}$), and no self- or cross-phase modulation ($\alpha = 0$). In this ideal case, one can obtain analytical expressions for the maximum efficiency η^{\max} and critical powers, $P_0^{\text{crit}} = |s_{0+}^{\text{crit}}|^2$ and $P_m^{\text{crit}} = |s_{m+}^{\text{crit}}|^2$, at which 100% depletion of the total input power is attained [41]. Performing a similar calculation, but this time

including the possibility of losses, we find:

$$P_0^{\text{crit}} = \frac{4}{\tau_{s0}|\beta_0|\sqrt{\tau_m\tau_p}\omega_m\omega_p} \quad (10)$$

$$\eta^{\text{max}} = \frac{\tau_p}{\tau_{sp}} \left(2 - \frac{\tau_{s0}}{\tau_0} \right) \frac{\omega_p}{2\omega_0}. \quad (11)$$

With respect to the lossless case, the presence of losses merely decreases the maximum achievable efficiency by a factor of $\tau_p/\tau_{sp}(2 - \tau_{s0}/\tau_0)$ while increasing the critical power P_0^{crit} by a factor of $\sqrt{\tau_{sm}\tau_{sp}/\tau_m\tau_p}$. As in the case of no losses, 100% depletion is only possible in the limit as $P_m \rightarrow 0$, from which it follows that the maximum efficiency is independent of τ_m . As noted in [41], the existence of a limiting efficiency (Eq. 11) can also be predicted from the Manley–Rowe relations governing energy transfer in nonlinear systems [68] as can the limiting condition $P_m \rightarrow 0$. While theoretically this suggests that one should always employ as small a P_m as possible, as we show below, practical considerations make it desirable to work at a small but finite (non-negligible) P_m .

B. Self- and cross-phase modulation

Unlike losses, the presence of self- and cross-phase modulation dramatically alters the frequency-conversion process. Specifically, a finite α leads to a power-dependent shift in the effective cavity frequencies $\omega_{ck}^{\text{NL}} = \omega_{ck}(1 - \sum_j \alpha_{kj}|A_j|^2)$ that spoils both the frequency-matching condition as well as the coupling of the incident light to the corresponding cavity modes. One approach to overcome this difficulty is to choose/design the linear cavity frequencies to have frequency ω_{ck} slightly detuned from the incident frequencies ω_k , such that at the critical powers, the effective cavity frequencies align with the incident frequencies and satisfy the frequency matching condition [41]. Specifically, assuming incident light at ω_0 and ω_m , it follows by inspection of Eqs. 1–4 that pre-shifting the linear cavity resonances away from the incident frequencies according to the transformation,

$$\omega_{c0}^{\text{crit}} = \frac{\omega_0}{1 - \alpha_{00}|a_0^{\text{crit}}|^2 - \alpha_{0m}|a_m^{\text{crit}}|^2 - \alpha_{0p}|a_p^{\text{crit}}|^2} \quad (12)$$

$$\omega_{cm}^{\text{crit}} = \frac{\omega_m}{1 - \alpha_{m0}|a_0^{\text{crit}}|^2 - \alpha_{mm}|a_m^{\text{crit}}|^2 - \alpha_{mp}|a_p^{\text{crit}}|^2} \quad (13)$$

$$\omega_{cp}^{\text{crit}} = \frac{2\omega_0 - \omega_m}{1 - \alpha_{p0}|a_0^{\text{crit}}|^2 - \alpha_{pm}|a_m^{\text{crit}}|^2 - \alpha_{pp}|a_p^{\text{crit}}|^2}, \quad (14)$$

yields the same steady-state critical solution obtained for $\alpha = 0$, where a_k^{crit} denote the critical, steady-state cavity fields.

An alternative approach to excite the critical solution above in the presence of self- and cross-phase modulation is to detune the incident frequencies away from ω_{c0} and ω_{cm} , keeping the two cavity frequencies unchanged, while pre-shifting ω_{cp} to enforce frequency matching. Specifically, by inspection of Eqs. 12–14, it follows that choosing input-light frequencies

$$\omega_0^{\text{crit}} = \omega_{c0} (1 - \alpha_{00}|a_0^{\text{crit}}|^2 - \alpha_{0m}|a_m^{\text{crit}}|^2 - \alpha_{0p}|a_p^{\text{crit}}|^2) \quad (15)$$

$$\omega_m^{\text{crit}} = \omega_{cm} (1 - \alpha_{m0}|a_0^{\text{crit}}|^2 - \alpha_{mm}|a_m^{\text{crit}}|^2 - \alpha_{mp}|a_p^{\text{crit}}|^2), \quad (16)$$

and tuning ω_{cp} such that

$$\omega_{cp}^{\text{crit}} = \frac{2\omega_{c0}(1 - \sum \alpha_{0k}|a_k^{\text{crit}}|^2) - \omega_{cm}(1 - \sum \alpha_{mk}|a_k^{\text{crit}}|^2)}{1 - \sum \alpha_{pk}|a_k^{\text{crit}}|^2}, \quad (17)$$

yields the same steady-state critical solution above. This approach is advantageous in that the requirement that all three cavity frequencies be simultaneously and independently tuned (post-fabrication) is removed in favor of tuning a single cavity mode. Given a scheme to tune the frequencies of the cavity modes that achieves perfect frequency matching at the critical power, what remains is to analyze the stability and excitability of the new critical solution, which can be performed using a straightforward linear stability analysis of the coupled mode equations [38]. Before addressing these questions, however, it is important to address a more serious concern.

C. Frequency mismatch

Regardless of tuning mechanism, in practice one can never fully satisfy perfect frequency matching (even when self- and cross-phase modulation can be neglected) due to fabrication imperfections. In general, one would expect the finite bandwidth to mean that there is some tolerance $\sim 1/Q_p$ on any frequency mismatch $\Delta\omega = 2\omega_{c0} - \omega_{cm} - \omega_{cp} \lesssim \omega_{cp}/Q_{cp}$ [60]. However, here we find that instabilities and strong modifications of the cavity lineshapes arising from the particular nature of this nonlinear process lead to extreme, sub-bandwidth sensitivity to frequency deviations that must be carefully examined if one is to achieve high-efficiency operation.

To illustrate the effects of frequency mismatch, we first consider an ideal, lossless system with zero self- and cross-phase modulation ($\alpha = 0$) and with incident light at frequencies $\omega_0 = \omega_{c0}$ and $\omega_m = \omega_{cm}$, and powers P_0^{crit} and P_m , respectively. With the exception of α , the coupling coefficients and cavity parameters correspond to those of the 2d design described in Sec. III B. Figure 2 (top) shows the steady-state conversion efficiency η (solid lines) as a function of the frequency mismatch $\Delta_{cp} = \omega_{cp} - \omega_{cp}^{\text{crit}}$ away from perfect frequency-matching, for multiple values of $P_m = \{0.001, 0.01, 0.1\}P_0^{\text{crit}}$, with blue/red solid lines denoting stable/unstable steady-state fixed points. As shown, solutions come in pairs of stable/unstable fixed points, with the stable solution approaching the maximum-efficiency η^{max} critical solution as $P_m \rightarrow 0$. Moreover, one observes that as Δ_{cp} increases for finite P_m , the stable and unstable fixed points approach and annihilate one other, with limit cycles appearing in their stead (an example of what is known as a ‘‘saddle-node homoclinic bifurcation’’ [69]). The mismatch at which this bifurcation occurs is proportional to P_m , so that, as $P_m \rightarrow 0$, the regime over which there exist high-efficiency steady states reduces to a single *fixed point* occurring at $\Delta_{cp} = 0$. Beyond this bifurcation point, the system enters a limit-cycle regime (shaded regions) characterized by periodic modulations of the output signal in time [37, 38, 70]. Interestingly, we find that

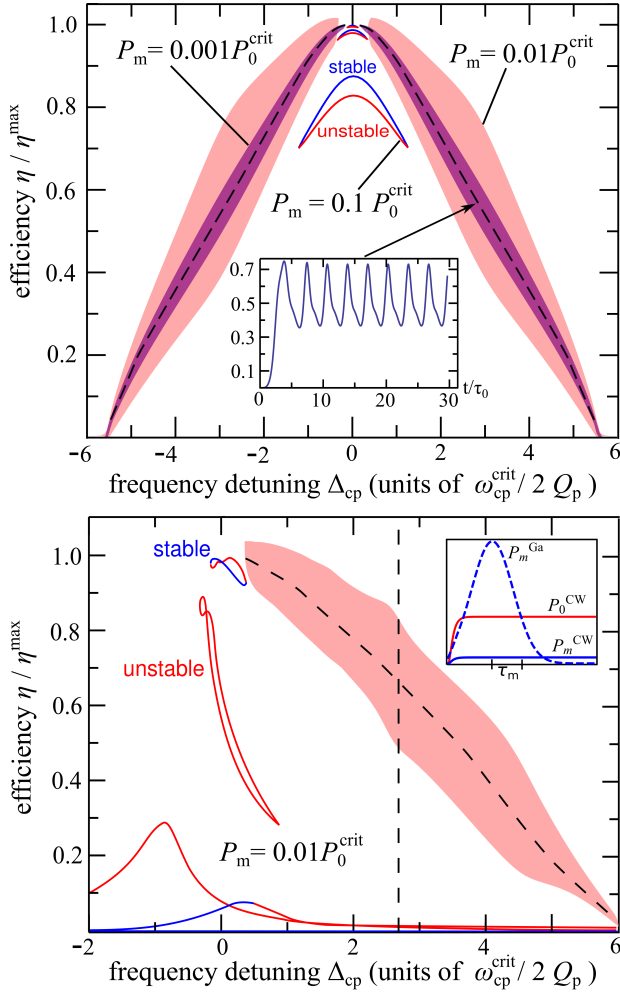


FIG. 2: (Top:) Steady-state conversion efficiency η (normalized by the maximum achievable efficiency η^{\max}) as a function of frequency mismatch $\Delta_{\text{cp}} = \omega_{\text{cp}} - \omega_{\text{cp}}^{\text{crit}}$ (in units of $\omega_{\text{cp}}^{\text{crit}}/2Q_{\text{p}}$), for the cavity system depicted in Fig. 4, but in the absence of self- and cross-phase modulation ($\alpha = 0$). Incident frequencies are chosen to be $\omega_0 = \omega_0^{\text{crit}}$ and $\omega_{\text{m}} = \omega_{\text{m}}^{\text{crit}}$, with corresponding powers $P_0 = P_0^{\text{crit}}$ and P_{m} , where we consider multiple $P_{\text{m}} = \{0.1, 0.01, 0.001\}P_0^{\text{crit}}$. Note that since $\alpha = 0$, critical frequencies are independent of incident powers, so that $\omega_0^{\text{crit}} = \omega_{\text{c}0}$, $\omega_{\text{m}}^{\text{crit}} = \omega_{\text{cm}}$, and $\omega_{\text{cp}}^{\text{crit}} = 2\omega_{\text{c}0} - \omega_{\text{cm}}$. Blue/red solid lines denote stable/unstable fixed points, whereas shaded areas indicate regimes lacking fixed point solutions and exhibiting limit-cycle behavior, shown only for $P_{\text{m}} = \{0.01, 0.001\}P_0^{\text{crit}}$, with smaller amplitudes corresponding to smaller P_{m} . Dashed lines denote the average efficiency of the limit cycles $\bar{\eta}$, whereas the top/bottom of the shaded regions denote the maximum/minimum efficiency per period. The inset shows the efficiency as a function of time for a typical limit cycle, obtained at $\Delta_{\text{cp}} \approx 3\omega_{\text{cp}}^{\text{crit}}/2Q_{\text{p}}$. (Bottom:) η and $\bar{\eta}$ for the same system above, but in the presence of self- and cross-phase modulation ($\alpha \neq 0$), and only for $P_{\text{m}} = 0.01P_0^{\text{crit}}$. Note that additional stable and unstable fixed points arise due to the non-zero α , and that limit-cycle behaviors arise only for $\Delta_{\text{cp}} > 0$. Inset shows the temporal shape of the incident power needed to excite the desired limit cycles, corresponding to a Gaussian pulse superimposed over CW inputs.

the average efficiency of the limit cycles (dashed lines),

$$\bar{\eta} = \lim_{T \rightarrow \infty} \frac{1}{T} \int_0^T dt \eta(t), \quad (18)$$

remains large and $\lesssim \eta^{\max}$ even as Δ_{cp} is several fractional bandwidths. The inset of Fig. 2 (top) shows the efficiency of this system as a function of time (in units of the lifetime τ_0) for large mismatch $\Delta_{\text{cp}} = 3\omega_{\text{cp}}^{\text{crit}}/2Q_{\text{p}}$. As expected, the modulation amplitude and period of the limit cycles depend on the input power and mismatch, and in particular we find that the amplitude goes to zero and the period diverges $\sim 1/\Delta_{\text{cp}}$ as $\Delta_{\text{cp}} \rightarrow 0$. This behavior is observed across a wide range of P_{m} , with larger P_{m} leading to lower $\bar{\eta}$ and larger amplitudes. For small enough mismatch, the modulation frequency enters the THz regime, in which case standard rectifications procedures [71] can be applied to extract the useful THz oscillations [4, 5, 72–75].

Frequency mismatch leads to similar effects for finite α , including homoclinic bifurcations and corresponding high-efficiency limit cycles that persist even for exceedingly large frequency mismatch. One important difference, however, is that the redshift associated with self- and cross-phase modulation creates a strongly asymmetrical lineshape that prevents high-efficiency operation for $\Delta_{\text{cp}} < 0$. Figure 2 (bottom) shows the stable/unstable fixed points (solid lines) and limit cycles (dashed regions) as a function of Δ_{cp} for the same system of Fig. 2 (top) but with finite α , for multiple values of $P_{\text{m}} = \{0.001, 0.01\}P_0^{\text{crit}}$. As before, the coupling coefficients and cavity parameters correspond to those of the 2d design described in Sec. III B. Here, in contrast to the $\alpha = 0$ case, the critical incident frequencies ω_0^{crit} and $\omega_{\text{m}}^{\text{crit}}$ are chosen according to Eqs. 15–16 in order to counter the effects of self- and cross-phase modulation, and are therefore generally different from $\omega_{\text{c}0}$ and ω_{cm} . Aside from the asymmetrical lineshape, one important difference from the $\alpha = 0$ case is the presence of additional stable/unstable low-efficiency solutions. Multi-stability complicates matters since, depending on the initial conditions, the system can fall into different stable solutions and in particular, simply turning on the source at the critical input power may result in an undesirable low-efficiency solution. One well-known technique that allows such a system to lock into the desired high-efficiency solutions is to superimpose a gradual exponential turn-on of the pump with a Gaussian pulse of larger amplitude [37]. We found that a single Gaussian pulse with a peak power of $4P_0^{\text{crit}}$ and a temporal width $\sim \tau_{\text{m}}$, depicted in the right inset of Fig. 2 (bottom), is sufficient to excite high-efficiency limit cycles in the regime $\Delta_{\text{cp}} > 0$.

Despite their high efficiencies (even for large $\Delta_{\text{cp}} \gtrsim 1$), the limit-cycle solutions above leave something to be desired. Depending on the application, it may be desirable to operate at high-efficiency fixed points. One way to achieve this for non-zero frequency mismatch is to abandon the critical solution and instead choose incidence parameters that exploit self- and cross-phase modulation in order to enforce perfect frequency

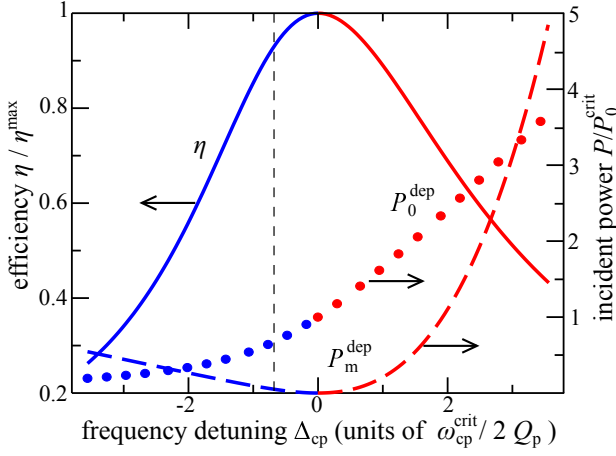


FIG. 3: Steady-state conversion efficiency (normalized by the maximum achievable efficiency η^{\max}) and required incident powers P_0^{dep} and P_m^{dep} (normalized by the critical power P_0^{crit}) corresponding to depleted steady states of the system of Fig. 4, as a function of frequency mismatch $\Delta_{\text{cp}} = \omega_{\text{cp}} - \omega_{\text{cp}}^{\text{crit}}$ (in units of $\omega_{\text{cp}}^{\text{crit}}/2Q_p$). As described in Sec. III B 2, depleted states yield 100% depletion of P_0 , and are excited by appropriate combinations of incident frequencies $\omega_k = \omega_k^{\text{dep}}$ and powers $P_k = P_k^{\text{dep}}$. Blue/red lines denote stable/unstable solutions, with solid and dashed lines, and circles, denoting η , P_m^{dep} , and P_0^{dep} , respectively.

matching and 100% depletion of the pump as follows,

$$\omega_{\text{cp}}^{\text{NL}} + \omega_{\text{cm}}^{\text{NL}} = 2\omega_{\text{c0}}^{\text{NL}}, \quad (19)$$

$$s_{0-} = 0 \quad (20)$$

Specifically, enforcing Eqs. 19–20 by solving Eqs. 1–4 for ω_0^{dep} , ω_m^{dep} , P_0^{dep} , and P_m^{dep} , we obtain a *depleted* steady-state solution a_k^{dep} that, in contrast to the critical solution a_k^{crit} , yields a steady-state efficiency that corresponds to 100% depletion of the pump regardless of frequency mismatch. Note that we are not explicitly maximizing the conversion efficiency but rather enforcing complete conversion of pump energy in the presence of frequency mismatch, at the expense of a non-negligible input P_m^{dep} . Figure 3 shows the depleted steady-state efficiency η^{dep} (solid line) and corresponding incident powers (solid circles and dashed line) as a function of Δ_{cp} , for the same system of Fig. 2 (bottom). We find that for most parameters of interest, depleted efficiencies and powers are uniquely determined by Eqs. 19–20. As expected, the optimal efficiency occurs at $\Delta_{\text{cp}} = 0$ and corresponds to the critical solution, so that $P_0^{\text{dep}} = P_0^{\text{crit}}$, $P_m^{\text{dep}} = P_m^{\text{crit}} = 0$, and $\eta^{\text{dep}} = \eta^{\max}$. For finite $\Delta_{\text{cp}} \neq 0$, the optimal efficiencies are lower due to the finite P_m^{dep} , but there exist a broad range of Δ_{cp} over which one obtains relatively high efficiencies $\sim \eta^{\max}$. Power requirements P_0^{dep} and P_m^{dep} follow different trends depending on the sign of Δ_{cp} . Away from zero detuning, P_m^{dep} can only increase whereas P_0^{dep} decreases for $\Delta_{\text{cp}} < 0$ and increases for $\Delta_{\text{cp}} > 0$. In the latter case, the total input power exceeds P_0^{crit} leading to the observed instability of the fixed-point solutions.

Finally, we point out that limit cycles and depleted steady states reside in roughly complementary regimes. Although no stable high-efficiency fixed points can be found in the $\Delta_{\text{cp}} > 0$ regime, it is nevertheless possible to excite high-efficiency limit cycles. Conversely, although no such limit cycles exist for $\Delta_{\text{cp}} < 0$, it is possible in that case to excite high-efficiency depleted steady states.

III. NANOBEAM DESIGNS

In this section, we consider concrete and realistic cavity designs in 2d and 3d, and check the predictions of our TCMT by performing exact nonlinear FDTD simulations in 2d. Our designs are based on a particular class of PhC nanobeam structures, depicted schematically in Figs. 4 and 8, where a cavity is formed by the introduction of a defect in a lattice of air holes in dielectric, and coupled to an adjacent waveguide formed by the removal of holes on one side of the defect. We restrict our analysis to dielectric materials with high nonlinearities at near- and mid-infrared wavelengths [1], and in particular focus on undoped silicon, whose refractive index $n \approx 3.4$ and Kerr susceptibility $\chi^{(3)} \sim 10^{-18} \text{ m}^2/\text{V}^2$ [76].

A. General design considerations

Before delving into the details of any particular design, we first describe the basic considerations required to achieve the desired high efficiency characteristics. To begin with, we require three modes satisfying the frequency-matching condition to within some desired bandwidth (determined by the smallest of the mode bandwidths). We begin with the linear cavity design, in which case we seek modes that approximately satisfy $\omega_{\text{cm}} + \omega_{\text{cp}} = 2\omega_{\text{c0}}$. The final cavity design, incorporating self- and cross-phase modulation, is then obtained by additional tuning of the mode frequencies as described above. Second, we seek modes that have large nonlinear overlap β , determined by Eq. 8. (Ideally, one would also optimize the cavity design to reduce α/β , but such an approach falls beyond the scope of this work.) Note that the overlap integral β replaces the standard “quasiphase matching” requirement in favor of constraints imposed by the symmetries of the cavity [1]. In our case, the presence of reflection symmetries means that the modes can be classified as either even or odd and also as “TE-like” ($\mathbf{E} \cdot \hat{\mathbf{z}} \approx 0$) or “TM-like” ($\mathbf{H} \cdot \hat{\mathbf{z}} \approx 0$) [77], and hence only certain combinations of modes will yield non-zero overlap. It follows from Eq. 8 that any combination of even/odd modes will yield non-zero overlap so long as \mathbf{E}_m and \mathbf{E}_p have the same parity, and as long as all three modes have similar polarizations: modes with different polarization will cause the term $\sim (\mathbf{E}_0^* \cdot \mathbf{E}_m)(\mathbf{E}_0^* \cdot \mathbf{E}_p)$ in Eq. 8 to vanish. Third, in order to minimize radiation losses, we seek modes whose radiation lifetimes are much greater than their total lifetimes, as determined by any desired operational bandwidth. In what follows, we assume operational bandwidths with $Q \sim 10^3$. Finally, we require that our system support a single input/output port for light to couple in/out of

the cavity, with coupling lifetimes $Q_{sk} \ll Q_{rk}$ in order to have negligible radiation losses.

B. 2d design

In what follows, we consider two different 2d cavities with different mode frequencies but similar lifetimes and coupling coefficients. (Note that by 2d we mean that electromagnetic fields are taken to be uniform in the z direction.) The two cavities follow the same backbone design shown in Fig. 4 which supports three TE-polarized modes ($\mathbf{H} \cdot \hat{\mathbf{z}} = 0$) with radiative lifetimes $Q_0^{\text{rad}} = 6 \times 10^4$, $Q_m^{\text{rad}} = 6 \times 10^4$, and $Q_p^{\text{rad}} = 3 \times 10^3$, and total lifetimes $Q_0 = 1200$, $Q_m = 1100$, and $Q_p = 700$, respectively. The nonlinear coupling coefficients are calculated from the linear modal profiles (shown on the inset of Fig. 4) via Eqs. 8–7, and are given by:

$$\beta = (23.69 + 5.84i) \times 10^{-5} \left(\frac{\chi^{(3)}}{\epsilon_0 a^2 h} \right),$$

$$\begin{aligned} \alpha_{00} &= 4.935 \times 10^{-4} \left(\frac{\chi^{(3)}}{\epsilon_0 a^2 h} \right), \quad \alpha_{mm} = 5.096 \times 10^{-4} \left(\frac{\chi^{(3)}}{\epsilon_0 a^2 h} \right), \\ \alpha_{pp} &= 4.593 \times 10^{-4} \left(\frac{\chi^{(3)}}{\epsilon_0 a^2 h} \right), \quad \alpha_{0m} = 6.540 \times 10^{-4} \left(\frac{\chi^{(3)}}{\epsilon_0 a^2 h} \right), \\ \alpha_{0p} &= 5.704 \times 10^{-4} \left(\frac{\chi^{(3)}}{\epsilon_0 a^2 h} \right), \quad \alpha_{mp} = 5.616 \times 10^{-4} \left(\frac{\chi^{(3)}}{\epsilon_0 a^2 h} \right), \end{aligned}$$

where the additional factor of h allows comparison to the realistic 3d structure below and accounts for finite nanobeam thickness (again, assuming uniform fields in the z direction). Compared to the optimal $\beta^{\text{max}} = \frac{3}{4n^4 w d} \left(\frac{\chi^{(3)}}{\epsilon_0 h} \right)$, corresponding to modes with uniform fields inside and zero fields outside the cavity, we find that $\beta = 5.5 \times 10^{-3} \beta^{\text{max}}$ is significantly smaller due to the fact that these TE modes are largely concentrated in air. In the 3d design section below, we choose modes with peaks in the dielectric regions, which leads to much larger $\beta \approx 0.4 \beta^{\text{max}}$.

In order to arrive at this 2d design, we explored a wide range of defect parameters, with the defect formed by modifying the radii of a finite set of holes in an otherwise periodic lattice of air holes of period a and radius $R = 0.36a$ in a dielectric nanobeam of width $w = 1.2a$ and index of refraction $n = 3.4$. The defect was parametrized via an exponential adiabatic taper of the air-hole radii r , in accordance with the formula $r(x) = R \left(1 - \frac{3}{4} e^{-\frac{4|x|^2}{d^2}} \right)$, where the parameter d is an “effective cavity length”. Such an adiabatic taper is chosen to reduce radiation/scattering losses at the interfaces of the cavity [78]. The removal of holes on one side of the defect creates a waveguide, with corresponding cavity–waveguide coupling lifetimes Q_{sk} determined by the number of holes removed [79–81]. To illustrate the dependence of the mode properties on the cavity parameters, Fig. 5(top) shows the evolution of the cavity-mode frequencies as a function of d , with blue/red dots denoting even/odd modes and with larger dots denoting longer modal lifetimes. As expected, the volumes of the modes decrease with decreasing d , leading to larger β

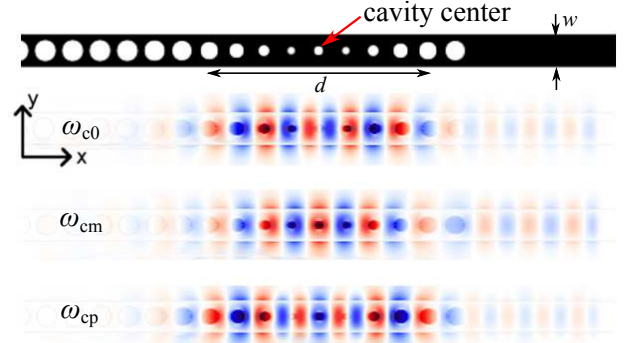


FIG. 4: Schematic of two-dimensional, triply-resonant cavity design involving a PhC nanobeam of refractive index $n = 3.4$, width $w = 1.2a$ and adiabatically varying hole radii (see text). The effective cavity length $d = 6.6a$ and the radius of the central hole R_0 are chosen so as to fine-tune the relative frequency spacing and lifetimes of the modes. Also shown are the E_y electric field components of the three modes relevant to DFWM. The cavity is coupled to a waveguide formed by the removal of holes to the right of the defect.

(smaller critical powers) but causing the frequency gap between the modes and radiation losses to increase. We find that the desired modal parameters for FWM lie at some intermediate $d \approx 6.6a$. In order to tune the relative frequencies between the modes, an additional tuning parameter is required. Specifically, it follows from perturbation theory [61] that changing the central hole radius R_0 allows control of the even-mode frequencies while leaving odd-mode frequencies unchanged. Figure 5(bottom) shows the evolution of the cavity-mode frequencies as a function of R_0 , for a fixed $d = 6.6a$. As described below, the particular choice of R_0 will depend on whether one seeks to operate with high-efficiency limit cycles versus high-efficiency steady-state solutions.

1. Limit cycles

In this section, we consider a design supporting high-efficiency limit cycles. Choosing $R_0 = 0.149a$, we obtain critical parameters $\omega_0^{\text{crit}} = 0.2319 \left(\frac{2\pi c}{a} \right)$, $\omega_m^{\text{crit}} = 0.2121 \left(\frac{2\pi c}{a} \right)$, $\omega_{cp}^{\text{crit}} = 0.2530 \left(\frac{2\pi c}{a} \right)$, and $P_0^{\text{crit}} = 10^{-3} \left(\frac{2\pi c \epsilon_0 a h}{\chi^{(3)}} \right)$, corresponding to frequency mismatch $\Delta_{cp} \approx 3\omega_{cp}^{\text{crit}}/2Q_p$ and critical efficiency $\eta^{\text{max}} = 0.51$. Choosing a small but finite $P_m = 0.01 P_0^{\text{crit}}$, it follows from Fig. 2 (dashed line) that the system will support limit cycles with average efficiencies $\bar{\eta} \approx 0.65 \eta^{\text{max}}$. To excite these solutions, we employed the priming technique described in Sec. II C. Figure 6 shows $\bar{\eta}$ as a function of P_0 , for incident frequencies $\omega_k = \omega_k^{\text{crit}}$ determined by Eqs. 15–16, as computed by our TCMT (gray line) and by exact, nonlinear FDTD simulations (solid circles). The two show excellent agreement. For $0.7 < P_0/P_0^{\text{crit}} < 3$, we observe limit cycles with relatively high $\bar{\eta}$, in accordance with the TCMT predictions, whereas outside of this regime, we find that the system invariably falls into low-efficiency fixed points. The periodic modulation of

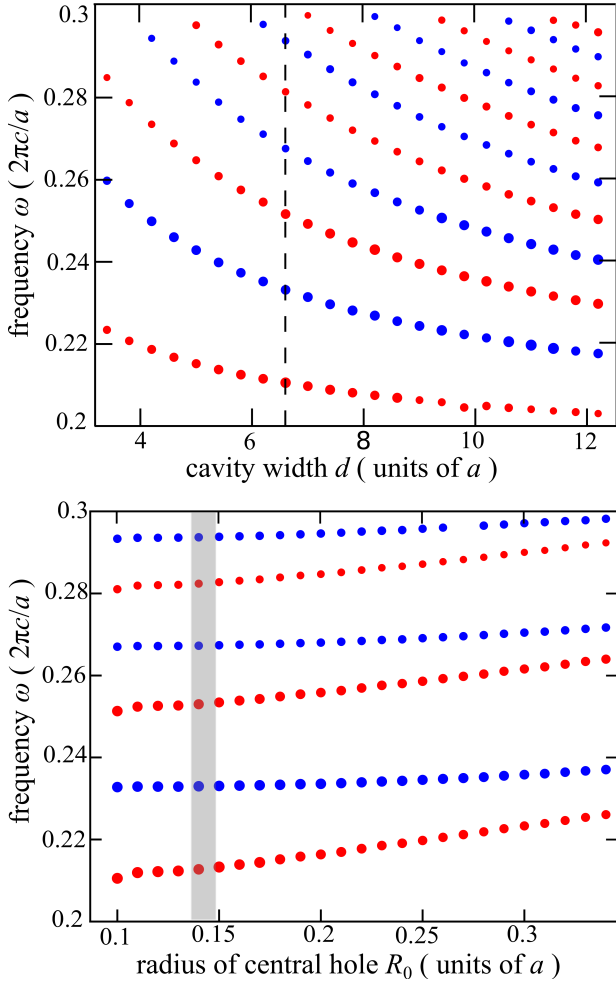


FIG. 5: Mode frequencies (in units of $2\pi c/a$) as a function of effective cavity length d (top), for fixed center-hole radius $R_0 = 0.9a$, and as a function of R_0 (bottom), for fixed $d = 6.6a$. Red/blue circles indicate symmetric/anti-symmetric mode profiles, where the size of the circle is proportional to the modal lifetime (quality factor) of the corresponding mode. The shaded area indicates the parameter region explored in the Sec. B1, B2.

the limit cycles means that instead of a single peak, the spectrum of the output signal consists of a set of equally spaced peaks surrounding ω_p . The top and bottom insets of Fig. 6 show the corresponding frequency spectra of the TCMT and FDTD output signals around ω_p , for a particular choice of $P_0 \approx P_0^{\text{crit}}$ (red circle), showing agreement both in the relative magnitude and spacing $\approx 2.5 \times 10^{-3} \left(\frac{2\pi c}{a}\right)$ of the peaks.

2. Depleted steady states

In this section, we consider a design supporting high-efficiency, depleted steady states. Choosing $R_0 = 0.143a$, one obtains critical parameters $\omega_0^{\text{crit}} = 0.2320 \left(\frac{2\pi c}{a}\right)$, $\omega_m^{\text{crit}} = 0.2118 \left(\frac{2\pi c}{a}\right)$, $\omega_{\text{cp}}^{\text{crit}} = 0.2532 \left(\frac{2\pi c}{a}\right)$, and $P_0^{\text{crit}} = 10^{-3} \left(\frac{2\pi c \epsilon_0 a h}{\chi^{(3)}}\right)$, corresponding to frequency mismatch $\Delta_{\text{cp}} \approx$

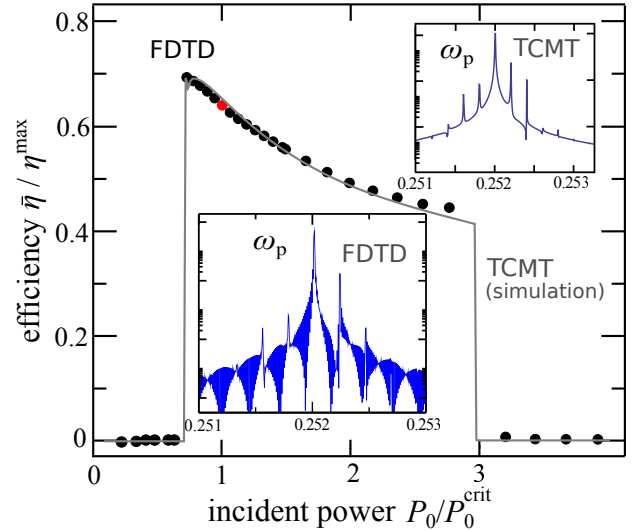


FIG. 6: Average conversion efficiency $\bar{\eta}$ (normalized by the maximum achievable efficiency η^{max}) of limit cycles as a function of power P_0 (normalized by P_0^{crit}) at the critical frequencies ω_0^{crit} and ω_m^{crit} and a fixed $P_m = 0.01P_0^{\text{crit}}$. The modal parameters are obtained from the 2d cavity of Fig. 4, with chosen $R_0 = 0.149a$ leading to a detuning $\Delta_{\text{cp}} \approx 3\omega_{\text{cp}}^{\text{crit}}/2Q_p$ corresponding to the dashed line in Fig. 2 (bottom). Solid circles and gray lines denote results as computed by FDTD and TCMT. Insets show the spectra of the output light for a given P_0 (red circle), and for both FDTD and TCMT.

$-0.6\omega_{\text{cp}}^{\text{crit}}/2Q_p$ and critical efficiency $\eta^{\text{max}} = 0.51$. Choosing incident frequencies $\omega_0^{\text{dep}} = 0.2320 \left(\frac{2\pi c}{a}\right)$, $\omega_m^{\text{dep}} = 0.2119 \left(\frac{2\pi c}{a}\right)$, and incident powers $P_0^{\text{dep}} \approx 0.7P_0^{\text{crit}}$ and $P_m^{\text{dep}} \approx 0.04P_0^{\text{crit}}$, it follows from Fig. 3 (dashed line) that the system supports stable, depleted steady states with efficiencies $\approx 0.95\eta^{\text{max}}$. Figure 7 shows the efficiency of the system as a function P_0 , with all other incident parameters fixed to the depleted-solution values above, where blue/red lines denote stable/unstable solutions. As before, we employ the priming technique of Sec. II C in order to excite the desired high efficiency solutions and obtain excellent agreement between our TCMT (gray line) and FDTD simulations (solid circles). Exciting the high-efficiency solutions by steady-state input “primed” with a Gaussian pulse is convenient in FDTD because it leads to relatively short simulations, but is problematic for $P_0 > 0.8P_0^{\text{crit}}$, where the system becomes very sensitive to the priming parameters, and it became impractical in for us to find the optimal FDTD source conditions in Fig. 7. In realistic experimental situations, however, one can use a different technique to excite the high-efficiency solution in a way that is very robust to errors, based on adiabatic tuning of the pump power [37].

C. 3d design

We now consider a 3d design, depicted in Fig. 8, as a feasible candidate for experimental realization. The cavity supports three TE_{00} modes ($\mathbf{E}_z = 0$ at $z = 0$) of fre-

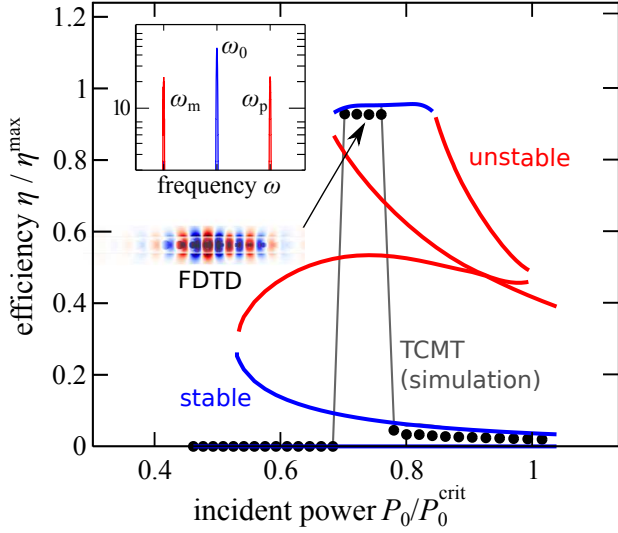


FIG. 7: Conversion efficiency η (normalized by the maximum achievable efficiency η^{\max}) of depleted states as a function of power P_0 (normalized by P_0^{crit}), at incident frequencies ω_0^{dep} and ω_m^{dep} , and a fixed power $P_m^{\text{dep}} \approx 0.2P_0^{\text{crit}}$. The modal parameters are obtained from the 2d cavity of Fig. 4, with $R_0 = 0.143a$ leading to a detuning $\Delta_{\text{cp}} \approx -0.6\omega_{\text{cp}}^{\text{crit}}/2Q_p$ corresponding to the dashed line in Fig. 3. E_y component of the steady-state electric field inside the cavity is shown as an inset (left-bottom). Solid circles and gray lines denote FDTD and TCMT, while blue/red lines denote stable/unstable steady states. Inset (left-top) shows the spectral profile (in arbitrary units) of the system, showing full depletion of the pump (blue) and correspondingly high conversion of the signal/idler frequencies (red). For $P_0 \gtrsim 0.8P_0^{\text{crit}}$, the system becomes ultra sensitive to the priming parameters, in which case high-efficiency solutions can only be excited by adiabatic tuning of the pump power (see text).

frequencies $\omega_{c0} = 0.2848 \left(\frac{2\pi c}{a}\right)$, $\omega_{\text{cm}} = 0.2801 \left(\frac{2\pi c}{a}\right)$ and $\omega_{\text{cp}} = 0.2895 \left(\frac{2\pi c}{a}\right)$, radiative lifetimes $Q_0^{\text{rad}} = 10^6$, $Q_m^{\text{rad}} = 3 \times 10^4$, $Q_p^{\text{rad}} = 2 \times 10^4$. As before, the total lifetimes can be adjusted by removing air holes to the right or left of the defect, which would allow coupling to the resulting in-plane waveguides. (Alternatively, one might consider an out-of-plane coupling mechanism in which a fiber carrying incident light at both ω_0 and/or ω_m is brought in close proximity to the cavity [79, 82].) In what follows, we do not consider any one particular coupling channel and focus instead on the isolated cavity design. Nonlinear coupling coefficients are calculated from the linear modal profiles (shown on the inset of Fig. 8) via Eqs. 9–7, and are given by:

$$\beta = 2 \times 10^{-4} \left(\frac{\chi^{(3)}}{\epsilon_0 a^3} \right),$$

$$\alpha_{00} = 8.1 \times 10^{-4} \left(\frac{\chi^{(3)}}{\epsilon_0 a^3} \right), \quad \alpha_{\text{mm}} = 4.6 \times 10^{-4} \left(\frac{\chi^{(3)}}{\epsilon_0 a^3} \right),$$

$$\alpha_{\text{pp}} = 11.5 \times 10^{-4} \left(\frac{\chi^{(3)}}{\epsilon_0 a^3} \right), \quad \alpha_{0\text{m}} = 6.2 \times 10^{-4} \left(\frac{\chi^{(3)}}{\epsilon_0 a^3} \right),$$

$$\alpha_{0\text{p}} = 12.7 \times 10^{-4} \left(\frac{\chi^{(3)}}{\epsilon_0 a^3} \right), \quad \alpha_{\text{mp}} = 5.5 \times 10^{-4} \left(\frac{\chi^{(3)}}{\epsilon_0 a^3} \right).$$

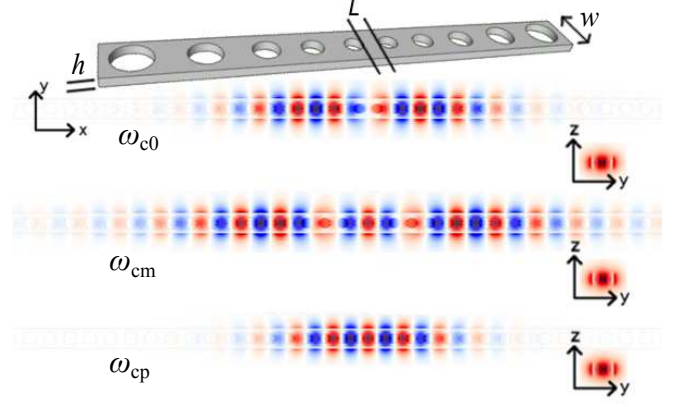


FIG. 8: Schematic of three dimensional, triply resonant cavity design involving a PhC nanobeam of refractive index $n = 3.4$, width $w = a$, and height $h = 0.51a$, and linearly tapered air holes, as described in the text. The central cavity length $L \approx 0.4a$ and number of taper segments are chosen so as to fine-tune the relative frequency spacing and lifetimes of the modes. Also shown are the E_y electric-field components of three TE-like modes with fundamental TE00 transverse profiles, and with frequencies $\omega_{c0} = 0.2848 \left(\frac{2\pi c}{a}\right)$, $\omega_{\text{cm}} = 0.2801 \left(\frac{2\pi c}{a}\right)$ and $\omega_{\text{cp}} = 0.2895 \left(\frac{2\pi c}{a}\right)$. Radiation lifetimes are found to be $Q_0^{\text{rad}} = 10^6$, $Q_m^{\text{rad}} = 3 \times 10^4$, and $Q_p^{\text{rad}} = 2 \times 10^4$.

Here, in contrast to the 2d design of Sec. III B, we chose modes whose amplitudes are concentrated in dielectric regions, and therefore find appreciably larger $\beta \approx 0.4\beta^{\text{max}}$.

In order to arrive at the above 3d design, we explored a cavity parametrization similar to the one described in [83]. Specifically, we employed a suspended nanobeam of width $w = a$, thickness $h = 0.51a$, and refractive index $n = 3.4$. The beam is schematically divided into a set of $2N$ lattice segments, each having length $a_i, i \in \{\pm 1, \dots, \pm N\}$ and corresponding air-hole radii $R_i = 0.3a_i$, where $a_1 (a_{-1})$ is the length of the lattice segment immediately to the right (left) of the beam's center. The cavity defect is induced via a linear taper of a_i over a chosen set of $2\bar{N}$ segments, according to the formula:

$$a_i = a \left(f_a + \frac{(1-f_a)}{(\bar{N}-1)} (|i|-1) \right), \quad |i| \leq \bar{N}$$

$$= a, \quad |i| > \bar{N}.$$

In order to arrive at our particular design, we chose $f_a = 0.85$, $N = 21$, $\bar{N} = 9$ and varied the central cavity length L to obtain the desired TE₀₀ modes. Assuming total modal lifetimes $Q_0 = 8500$, $Q_m = 3000$, and $Q_p = 3000$ and using these design parameters, we obtain critical parameters $\omega_0^{\text{crit}} = 0.2843 \left(\frac{2\pi c}{a}\right)$, $\omega_m^{\text{crit}} = 0.2798 \left(\frac{2\pi c}{a}\right)$, $\omega_{\text{cp}}^{\text{crit}} = 0.2895 \left(\frac{2\pi c}{a}\right)$, and $P_0^{\text{crit}} = 5 \times 10^{-5} \left(\frac{2\pi c \epsilon_0 a^2}{\chi^{(3)}}\right)$, corresponding to frequency mismatch $\Delta_{\text{cp}} \approx -0.07\omega_{\text{cp}}^{\text{crit}}/(2Q_p)$ and $\eta^{\max} = 0.42$. Note that because the radiative losses in this system are non-negligible, the maximum efficiency of this system is $\approx 82\%$ of the optimal achievable efficiency $\omega_p/(2\omega_0) \approx 0.51$. At these small Δ_{cp} , we find that depletion of the pump is readily achieved through the critical parameters associated with perfect frequency matching. However, as illustrated in Sec. III B 1, it is indeed possible to choose a design that leads to highly efficient limit cycles or other dynamical behaviors.

We now express the power requirements of this particular design using real units instead of the dimensionless units of $2\pi c\epsilon_0 a^2/\chi^{(3)}$ we have employed thus far. Choosing to operate at telecom wavelengths $\lambda_{c0} \equiv 2\pi c/\omega_{c0} = 1.5\mu\text{m}$, with corresponding $n \approx 3.4$ and $\chi^{(3)} = 2.8 \times 10^{-18} \frac{\text{m}^2}{\text{V}^2}$ [1], we find that $a = 0.2848 \times 1500 = 427\text{nm}$ and $P_0^{\text{crit}} \approx 50\text{mW}$. Although our analysis above incorporates effects arising from linear losses (e.g. due to material absorption or radiation), it neglects important and detrimental sources of nonlinear losses in the telecom range, including two-photon and free carrier absorption [84, 85]. Techniques that mitigate the latter exist, e.g. reverse biasing [86], but in their absence it may be safer to operate in the spectral region below the half-bandgap of silicon [76]. One possibility is to operate at $\lambda_{c0} = 2.2\mu\text{m}$, in which case $\chi^{(3)} \approx 1.5 \times 10^{-18} \frac{\text{m}^2}{\text{V}^2}$ [76], leading to $a = 627\text{nm}$ and $P_0^{\text{crit}} \approx 200\text{mW}$. For a more detailed analysis of nonlinear absorption in triply resonant systems, the reader is referred to Ref. 87. While that work does not consider the effects of nonlinear dispersion, self- and cross-phase modulation, or frequency mismatch, it does provide upper bounds on the maximum efficiency in the presence of two-photon and free-carrier absorption.

IV. CONCLUDING REMARKS

In conclusion, using a combination of TCMT and FDTD simulations, we have demonstrated the possibility of achieving highly effi-

cient DFWM at low input powers ($\sim 50\text{mW}$) and large bandwidths ($Q \sim 1000$) in a realistic and chip-scale (μm) nanophotonic platform consisting of a triply resonant silicon nanobeam cavity. Our theoretical analysis includes detrimental effects stemming from linear losses, self- and cross-phase modulation, and mismatch of the cavity mode frequencies (e.g. arising from fabrication imperfections), and is checked against the predictions of a full nonlinear Maxwell FDTD simulation. Although power requirements in the tens of mW s are not often encountered in conventional chip-scale silicon nanophotonics, they are comparable if not smaller than those employed in conventional centimeter-scale DFWM schemes [86, 88, 89]. Our proof-of-concept design demonstrates that full cavity-based DFWM not only reduces device dimensions down to μm scales, but also allows depletion of the pump with efficiencies close to unity. However, we emphasize that there is considerable room for additional design optimization. In particular, we find that increasing the radiative lifetimes of the signal and converted modes (currently almost two orders of magnitudes lower than the pump) can significantly lower the power requirements of the system.

Acknowledgements: We acknowledge support from the MIT Undergraduate Research Opportunities Program and the U.S. Army Research Office through the Institute for Soldier Nanotechnology under contract W911NF-13-D-0001.

-
- [1] R. W. Boyd, *Nonlinear Optics* (Academic Press, California, 1992).
 - [2] J. Hald, *Optics Communications* **197**, 169 (2001).
 - [3] R. Lifshitz, A. Arie, and A. Bahabad, *Phys. Rev. Lett.* **95**, 133901 (2005).
 - [4] Y. A. Morozov, I. S. Nefedov, V. Y. Aleshkin, and I. V. Krasnikova, *Semiconductors* **39**, 113 (2005).
 - [5] K.-L. Yeh, M. C. Hoffmann, J. Hebling, and K. A. Nelson, *Applied Physics Letters* **90**, 171121 (pages 3) (2007).
 - [6] J. Hebling, A. G. Stepanov, G. Almasi, B. Bartal, and J. Kuhl, *Appl. Phys. B* **78**, 593 (2004).
 - [7] Z. Ruan, G. Veronis, K. L. Vodopyanov, M. M. Fejer, and S. Fan, *Opt. Express* **17**, 13502 (2009).
 - [8] R. H. Stolen and J. E. Bjorkholm, *IEEE J. Quantum Electron.* **18**, 1062 (1982).
 - [9] N. M. Kroll, *Phys. Rev.* **127**, 1207 (1962).
 - [10] R. H. Stolen, E. P. Ippen, and A. R. Tynes, *Appl. Phys. Lett.* **20**, 62 (1972).
 - [11] S. A. Akhmanov, A. P. Sukhorukov, and R. V. Khokhlov, *Soviet Physics JETP* **23**, 6 (1966).
 - [12] R. A. Fisher, *Optical phase conjugation* (Academic Press, Inc, New York, 1983).
 - [13] G. Contestabile, M. Presi, and E. Ciaramella, *IEEE Photon. Tech. Lett.* **16**, 7 (2004).
 - [14] S. J. B. Yoo, *J. Lightwave Tech.* **14**, 6 (1996).
 - [15] K. Gallo and G. Assanto, *Appl. Phys. Lett.* **79**, 3 (2001).
 - [16] H. Lira, Z. Yu, S. Fan, and M. Lipson, *Phys. Rev. Lett.* **109**, 033901 (2012).
 - [17] Y. Akahane, T. Asano, B.-S. Song, and S. Noda, *Nature* **425**, 944 (2003).
 - [18] V. R. Almeida, C. A. Barrios, R. R. Panepucci, and M. Lipson, *Nature* **431**, 1081 (2004).
 - [19] Y. A. Vlasov, M. O'Boyle, H. F. Hamann, and S. J. McNab, *Nature* **438**, 65 (2005).
 - [20] B.-S. Song, S. Noda, T. Asano, and Y. Akahane, *Nature Materials* **4**, 207 (2005).
 - [21] P. B. Deotare, M. W. McCutcheon, I. W. Frank, M. Khan, and M. Loncar, *Appl. Phys. Lett.* **94**, 121106 (2009).
 - [22] T. J. Kippenberg, S. M. Spillane, and K. J. Vahala, *Phys. Rev. Lett.* **93**, 083904 (2004).
 - [23] A. Rodriguez, M. Soljačić, J. D. Joannopoulos, and S. G. Johnson, *Opt. Express* **15**, 7303 (2007).
 - [24] M. Soljačić, M. Ibanescu, S. G. Johnson, Y. Fink, and J. D. Joannopoulos, *Phys. Rev. E Rapid Commun.* **66**, 055601(R) (2002).
 - [25] V. S. Ilchenko, A. A. Savchenkov, A. B. Matsko, and L. Maleki, *Phys. Rev. Lett.* **92**, 043903 (2004).
 - [26] J. U. Fürst, D. V. Strekalov, D. Elser, M. Lassen, U. L. Andersen, C. Marquardt, and G. Leuchs, *Phys. Rev. Lett.* **104**, 153901 (2010).
 - [27] X. Liu, R. M. Osgood, Y. A. Vlasov, and W. M. J. Green, *Nature Photonics* **4**, 557 (2010).
 - [28] M. A. Foster, A. C. Turner, J. E. Sharping, B. S. Schmidt, M. Lipson, and A. L. Gaeta, *Nature* **441**, 960 (2006).
 - [29] M. Bieler, *IEEE J. Select. Top. Quant. Electron.* **14**, 458 (2008).
 - [30] R. E. Hamam, M. Ibanescu, E. J. Reed, P. Bermel, S. G. Johnson, E. Ippen, J. D. Joannopoulos, and M. Soljagic, *Opt. Express* **12**, 2102 (2008).
 - [31] P. Bermel, A. Rodriguez, J. D. Joannopoulos, and M. Soljagic, *Phys. Rev. Lett.* **99**, 053601 (2007).
 - [32] J. Bravo-Abad, S. Fan, S. G. Johnson, J. D. Joannopoulos, and M. Soljagic, *J. Lightwave Tech.* **25**, 2539 (2007).
 - [33] L. Caspani, D. Duchesne, K. Dolgaleva, S. J. Wagner, M. Ferrera, L. Razzari, A. Pasquazi, M. Peccianti, D. J. Moss, J. S.

- Aitchison, et al., *J. Opt. Soc. Am. B* **28**, A67 (2011).
- [34] F. S. Felber and J. H. Marburger, *Appl. Phys. Lett.* **28**, 731 (1976).
- [35] Y. Dumeige and P. Feron, *Phys. Rev. A* **84**, 043847 (2011).
- [36] R. G. Smith, *IEEE J. Quantum Electron.* **6**, 215 (1970).
- [37] H. Hashemi, A. W. Rodriguez, J. D. Joannopoulos, M. Soljagic, and S. G. Johnson, *Phys. Rev. A* **79**, 013812 (2009).
- [38] P. D. Drummond, K. J. McNeil, and D. F. Walls, *Optica Acta* **27**, 321 (1980).
- [39] K. Grygiel and P. Szlachetka, *Opt. Comm.* **91**, 241 (1992).
- [40] E. Abraham, W. J. Firth, and J. Carr, *Physics Lett. A* pp. 47–51 (1982).
- [41] D. Ramirez, A. W. Rodriguez, H. Hashemi, J. D. Joannopoulos, M. Soljagic, and S. G. Johnson, *Phys. Rev. A* **83**, 033834 (2011).
- [42] K. R. Parameswaran, J. R. Kurz, R. V. Roussev, and M. M. Fejer, *Opt. Express* **27**, 1 (2002).
- [43] P. S. Kuo and G. S. Solomon, *Opt. Express* **19**, 16898 (2011).
- [44] M. Ferrera, L. Razzari, D. Duchesne, R. Morandotti, Z. Yang, M. Liscidini, J. E. Sipe, S. Chu, B. E. Little, and D. J. Moss, *Nature Photonics* **2**, 737 (2008).
- [45] P. P. Absil, J. V. Hryniewicz, B. E. Little, P. S. Cho, R. A. Wilson, L. G. Joneckis, and P.-T. Ho, *Opt. Lett.* **25**, 554 (2000).
- [46] Y. Dumeige and P. Feron, *Phys. Rev. A* **74**, 063804 (2006).
- [47] J. S. Levy, M. A. Foster, A. L. Gaeta, and M. Lipson, *Opt. Express* **19**, 11415 (2011).
- [48] K. Rivoire, S. Buckley, F. Hatami, and J. Vuckovic, *Appl. Phys. Lett.* **98**, 263113 (2011).
- [49] S. Buckley, M. Radulaski, K. Biermann, and J. Vuckovic, *ArXiv:1308.6051v1* (2013).
- [50] K. Rivoire, Z. Lin, F. Hatami, and J. Vuckovic, *Appl. Phys. Lett.* **97**, 043103 (2010).
- [51] B. Kuyken, S. Clemmen, S. K. Selvaraja, W. Bogaerts, D. V. Thourhout, P. Emplit, S. Massar, G. Roelkens, and R. Baets, *Opt. Lett.* **36**, 552 (2011).
- [52] T. Carmon and K. J. Vahala, *Nature* **3**, 430 (2007).
- [53] H. Fukuda, K. Yamada, T. Shoji, M. Takahashi, T. Tsuchizawa, T. Watanabe, J. Takahashi, and S. Itabashi, *Opt. Express* **13**, 4629 (2005).
- [54] S. Reza, M. A. Foster, A. C. Turner, D. F. Geraghty, M. Lipson, and A. L. Gaeta, *Nature Photonics* **2**, 35 (2008).
- [55] I. Agha, M. Davanco, B. Thurston, and K. Srinivasan, *Opt. Lett.* **37**, 2997 (2012).
- [56] P. Del’Haye, A. Schilegger, O. Arcizet, T. Wilken, R. Holzwarth, and T. J. Kippenberg, *Nature* **450**, 1214 (2007).
- [57] J. S. Levy, A. Gondarenko, M. A. Foster, A. C. Turner, A. L. Gaeta, and M. Lipson, *Nature Photonics* **4**, 37 (2010).
- [58] Y. Okawachi, K. Saha, J. S. Levy, Y. H. Wen, M. Lipson, and A. L. Gaeta, *Opt. Lett.* **36**, 3398 (2011).
- [59] I. B. Burgess, A. W. Rodriguez, M. W. McCutcheon, J. Bravo-Abad, Y. Zhang, S. G. Johnson, and M. Loncar, *OE* **17**, 9241 (2009).
- [60] Z.-F. Bi, A. W. Rodriguez, H. Hashemi, D. Duchesne, M. Loncar, K. Wang, and S. G. Johnson, *Opt. Express* **20**, 7 (2012).
- [61] J. D. Joannopoulos, R. D. Meade, and J. N. Winn, *Photonic Crystals: Molding the Flow of Light* (Princeton Univ. Press, 1995).
- [62] C. Sauvan, G. Lecamp, P. Lalanne, and J. P. Hugonin, *Opt. Express* **13**, 245 (2005).
- [63] A. R. M. Zain, N. P. Johnson, M. Sorel, and R. M. DeLaRue, *Opt. Express* **16**, 12084 (2008).
- [64] M. W. McCutcheon and M. Loncar, *Opt. Express* **16**, 19136 (2008).
- [65] M. Notomi, E. Kuramochi, and H. Taniyama, *Opt. Express* **16**, 11095 (2008).
- [66] Y. Zhang, M. W. McCutcheon, I. B. Burgess, and M. Loncar, *Opt. Lett.* **34**, 17 (2009).
- [67] Q. Quan and M. Loncar, *Opt. Express* **19**, 18529 (2011).
- [68] H. A. Haus, *Waves and Fields in Optoelectronics* (Prentice-Hall, Englewood Cliffs, NJ, 1984).
- [69] V. S. Afraimovich and L. P. Shilnikov, *Strange attractors and quasiattractors in Nonlinear Dynamics and Turbulence* (Pitman, New York, 1983).
- [70] S. H. Strogatz, *Nonlinear Dynamics and Chaos* (Westview Press, Boulder, CO, 1994).
- [71] M. Tonouchi, *Nature* **1** (2007).
- [72] Y. S. Lee, T. Meade, V. Perlin, H. Winful, T. B. Norris, and A. Galvanuskas, *Appl. Phys. Lett.* **76**, 2505 (2000).
- [73] K. L. Vodopyanov, M. M. Fejer, X. Xu, J. S. Harris, Y. S. Lee, W. C. Hurlbut, V. G. Kozlov, D. Bliss, and C. Lynch, *Appl. Phys. Lett.* **89**, 141119 (2006).
- [74] A. Andornico, J. Claudon, J. M. Gerard, V. Berger, and G. Leo, *Opt. Lett.* **33**, 2416 (2008).
- [75] J. Bravo-Abad, A. W. Rodriguez, J. D. Joannopoulos, P. T. Rakich, S. G. Johnson, and M. Soljagic, *Appl. Phys. Lett.* **96**, 101110 (2010).
- [76] Q. Lin, J. Zhang, G. Piredda, R. W. Boyd, P. M. Fauchet, and G. P. Agrawal, *Appl. Phys. Lett.* **91**, 021111 (2007).
- [77] J. D. Joannopoulos, S. G. Johnson, J. N. Winn, and R. D. Meade, *Photonic Crystals: Molding the Flow of Light* (Princeton University Press, 2008), 2nd ed., URL <http://ab-initio.mit.edu/book>.
- [78] M. Palamaru and P. Lalanne, *Appl. Phys. Lett.* **78**, 1466 (2001).
- [79] G.-H. Kim and Y.-H. Lee, *Opt. Express* **12**, 26 (2004).
- [80] A. Faraon, E. Waks, D. Englund, I. Fushman, and J. Vuckovic, *Appl. Phys. Lett.* **90**, 073102 (2007).
- [81] M. G. Banaee, A. G. Pattantyus-Abraham, M. W. McCutcheon, G. W. Rieger, and J. F. Young, *Appl. Phys. Lett.* **90**, 193106 (2007).
- [82] P. E. Barclay, K. Srinivasan, and O. Painter, *Opt. Express* **13**, 801 (2005).
- [83] P. B. Deotare, M. W. McCutcheon, I. W. Frank, M. Khan, and M. Loncar, *Appl. Phys. Lett.* **94**, 121106 (2009).
- [84] T. K. Liang and H. K. Tsang, *Appl. Phys. Lett.* **84**, 2745 (2004).
- [85] X. Yang and C. W. Wong, *Opt. Express* **15**, 4763 (2007).
- [86] H. Rong, Y.-H. Kuo, A. Liu, M. Paniccia, and O. Cohen, *Opt. Express* **14**, 1182 (2006).
- [87] X. Zeng and M. Popović, *ArXiv:1310.7078v1* (2013).
- [88] J. R. Ong, R. Kumar, R. Aguinaldo, and S. Mookherjea, *IEEE Photon. Tech. Lett.* **25**, 17 (2013).
- [89] K. Yamada, H. Fukuda, T. Tsuchizawa, T. Watanabe, T. Shoji, and S. Itabashi, *IEEE Photon. Tech. Lett.* **18**, 9 (2006).